AGU PUBLICATIONS

JGR

Journal of Geophysical Research: Space Physics

RESEARCH ARTICLE
10.1002/2015JA022054

Key Points:
- Physical mechanisms of fast and slow onsets of early VLF scattering events are explained
- Ion and electron chemistry is modeled during and following electric field heating
- O^- detachment can lead to continuous enhancement of the electron density for up to several seconds

Correspondence to:
D. A. Kotovsky,
dakotovsky@ufl.edu

Citation:
Kotovsky, D. A., and R. C. Moore (2016), Photochemical response of the nighttime mesosphere to electric field heating—Onset of electron density enhancements, *J. Geophys. Res. Space Physics*, *121*, 4782–4799, doi:10.1002/2015JA022054.

Received 20 OCT 2015
Accepted 17 MAR 2016
Accepted article online 23 MAR 2016
Published online 17 MAY 2016

Photochemical response of the nighttime mesosphere to electric field heating—Onset of electron density enhancements

D. A. Kotovsky[1] and R. C. Moore[1]

[1]Department of Electrical and Computer Engineering, University of Florida, Gainesville, Florida, USA

Abstract Onsets of electron density enhancements in the upper nighttime mesosphere produced by electric field heating of electrons are examined using a photochemical model that accounts for 29 dynamic species via a set of 156 reactions. Physical mechanisms are identified which result in electron density enhancements that continuously increase for up to several seconds after electric field heating, establishing the conditions under which early VLF scattering is either "fast" (<20 ms) or *slower* (>20 ms, including "slow," ≥500 ms). During heating, O^- ions are produced by heterolysis, $e^- + O_2 \rightarrow e^- + O^- + O^+$, and dissociative attachment, $e^- + O_2 \rightarrow O^- + O$. Following heating, a significant proportion of O^- ions associatively detach with molecular oxygen, $O^- + O_2 \rightarrow O_3 + e^-$, and atomic oxygen, $O^- + O \rightarrow O_2 + e^-$. If enough O^- ions are produced during heating such that O^- detachment exceeds electron loss (predominantly attachment, $e^- + O_3 \rightarrow O_2^- + O$, and/or electron-ion recombination), electron densities will continue to increase after heating has ended. Consequently, the total risetime of electron density enhancements produced by electric field heating is controlled by the duration of the electric field heating and (in some cases) the effects of O^- detachment following heating.

1. Introduction

Electric field changes due to lightning discharges are capable of directly affecting the overlying mesosphere and lower ionosphere, sometimes manifesting in the form of transient luminous events such as sprites [e.g., *Franz et al.*, 1990; *Lu et al.*, 2013], elves [e.g., *Boeck et al.*, 1992; *Newsome and Inan*, 2010], and sprite halos [e.g., *Barrington-Leigh et al.*, 2001; *Williams et al.*, 2012]. Lightning discharges are also capable of escaping thundercloud tops and propagating upward into the lower ionosphere; these are known as "gigantic jets" [e.g., *Pasko et al.*, 2002; *van der Velde et al.*, 2010]. Ionospheric conductivity changes which would directly result from lightning discharges (through either electric field changes or upward lightning discharges) can be remotely sensed via measurements of early VLF scattering events, which manifest as the perturbations of very low frequency (VLF, 3–30 kHz) subionospherically propagating radio waves.

Most early VLF scattering events exhibit onset durations less than 20 ms (i.e., "fast") [*Inan et al.*, 1996], which is the standard sampling period of many VLF narrowband observations. However, the works of *Haldoupis et al.* [2004, 2006] highlight a category of early VLF events which exhibit "slow" onset durations ranging from ~0.5 to ~2.5 s (for example of early/fast and early/slow events, see also *Kotovsky and Moore* [2015]). Previous reports of early VLF events with onset durations greater than 20 ms were presented by *Inan et al.* [1988, 1995]. Detection of multiple radio atmospherics throughout slow-onset durations of early VLF events were reported by *Inan et al.* [1995] and *Haldoupis et al.* [2006], leading those authors to support the suggestion of *Inan et al.* [1993] that multiple lightning strokes could be involved in altering the ionospheric conductivity associated with early/slow VLF events.

An early/slow VLF event for which the scattered field magnitude continued to rise for over a second after the most recently detected radio atmospheric or associated National Lightning Detection Network-recorded lightning flash was reported by *Kotovsky and Moore* [2015]. Additionally, they identified a number of early VLF events which exhibited onset durations ranging from 20 to 100 ms. Those observations indicate physical processes which result in slow (>20 ms) changes of ionospheric conductivity, and their possible association with persistent quasi-electrostatic field changes due to continuing currents or *M* components was suggested by the authors.

In modeling sprite halos, *Liu* [2012] demonstrated how electron densities beneath descending sprite halos can continue to increase while in the presence of electric fields lower than the local electric breakdown field (E_k). In subbreakdown electric fields, ionization rates are smaller than electron attachment rates (predominantly dissociative attachment with molecular oxygen forming O^-). Initially, electrons produced by ionization are quickly lost by attachment, producing O^-. However, as the density of O^- increases, O^- detachment rates increase, providing an additional source of electrons. Detachment rates of O^- are also enhanced by electric field heating. When the combined rates of ionization and detachment exceed rates of attachment, the densities of both electrons and O^- will increase. *Liu* [2012] modeled electron density growth beneath the descending halo which persisted for up to about 50 ms.

In this work, we demonstrate that O^- detachment *following* electric field heating of electrons can lead to continuous increase in the electron density for up to several seconds and may be partly or wholly responsible for the variety of early event onset durations reported by *Kotovsky and Moore* [2015]. In section 2, the photochemistry model utilized in this study is described. In section 3, mechanisms of O^- production and loss are discussed and simulated recoveries of O^- and e^- enhancements are shown which demonstrate the effect of O^- detachment on electron density growth. Also, in section 3, results of various simulations are shown demonstrating the importance of the electric field change waveshape and atmospheric conditions on electron density risetimes and magnitudes. In section 4 modeled risetimes of electron density enhancements due to O^- detachment are discussed in relation to onset durations of early VLF events.

2. Description of the Model

The photochemical model described herein is largely based upon the models of *Rowe et al.* [1974], *Thomas and Bowman* [1985], and *Sentman et al.* [2008] and has also been described in *Kotovsky and Moore* [2016]. The model includes a set of 156 reactions (Appendix A) applicable to the nighttime upper mesosphere (~70 to ~90 km) and is used to calculate the time dynamics of 29 chemical species. Dynamic species include 10 neutral species [$N_2(A)$, $N_2(B)$, $N_2(a')$, $N_2(C)$, $N(^4S)$, N^*, $O_2(a)$, $O_2(b)$, NO, and NO_2], electrons [e^-], 11 negative ion species [O^-, O_2^-, O_3^-, O_4^-, OH^-, CO_3^-, CO_4^-, NO_2^-, NO_3^-, $O_2^-{\cdot}NO$, and HCO_3^-], and 7 positive ion species [N_2^+, N^+, O_2^+, O^+, O_4^+, NO^+, and Y^+]. N^* is a set of nitrogen atoms in electronically excited states, and Y^+ is a set of positive cluster ions. Ambient sources of ionization include galactic cosmic radiation and photoionization. Details of these processes are given in subsections below.

Model calculations are performed at individual altitudes, independent of other altitudes (i.e., zero dimensional). Consequently, transport processes such as ambipolar, molecular, and eddy diffusion are not included in the calculations. Ambipolar diffusion loss is negligible for ions and electrons in the ambient ionosphere below approximately 150 km [*Whitten and Poppoff*, 1965, p. 125]. However, ambipolar diffusion may become important if electron or ion density gradients become large enough (for example, in ionization columns of sprites or gigantic jets). Molecular and eddy diffusion in the ambient nighttime ionosphere were shown to be important for odd nitrogen (N, NO, and NO_2) [e.g., *Strobel et al.*, 1970; *Sentman et al.*, 2008]. Consequently, the exclusion of molecular and eddy diffusion precludes the full calculation of odd nitrogen enhancement recoveries. However, the time scales of interest for this paper are much shorter than the chemical and transport lifetimes of odd nitrogen, which can be on the order of days or more in the ambient upper mesosphere [e.g., *Ogawa and Shimazaki*, 1975; *Frederick and Orsini*, 1982].

The remainder of this section will focus discussion on the determination and calculation of nighttime ambient profiles for the mesospheric chemical constituents. In order to simplify modeling efforts, nine neutral constituents [N_2, O_2, O, O_3, H_2O, H, OH, HO_2, and CO_2] were held constant during simulations. In the following, we discuss calculations performed in order to ensure that negligible error is introduced by holding these specific constituents constant over the time scales of interest for this paper.

A number of important neutral constituents are not in equilibrium throughout the nighttime upper mesosphere, including O, NO, H, OH, and HO_2 [e.g., *Ogawa and Shimazaki*, 1975; *Allen et al.*, 1984]. In order to obtain representative profiles suitable for simulations over the time scales of interest (tens of seconds or less), ambient neutral profiles for these constituents were adopted from other works. The NRLMSISE-00 model [*Picone et al.*, 2002] was utilized to obtain an atomic oxygen profile representative of nighttime summer conditions at midlatitudes, in addition to ambient profiles of N_2, O_2, and the neutral temperature (T_n). Midnight profiles for H, OH, and HO_2 were adopted from the diurnal calculations of *Allen et al.* [1984]. Additionally, an H_2O profile is adopted from the mixing ratios of [*Brasseur and Solomon*, 2005, p. 617], and a uniform CO_2 mixing

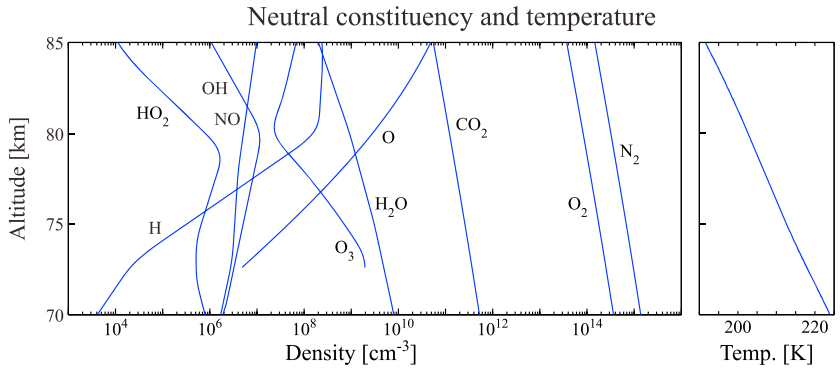

Figure 1. (left) Ambient profile of the nine static neutral constituents and NO. (right) Neutral temperature profile. Figure adapted from *Kotovsky and Moore* [2016].

ratio of 300 ppm is assumed. An ambient ozone profile is then calculated using the steady state balance reactions R157–R162 (see Appendix A for reactions). The ambient profiles of O and O_3 were found to be consistent with the midnight profiles of *Allen et al.* [1984], ensuring consistency between the odd oxygen and odd hydrogen constituents. Ambient profiles of these neutral species and the neutral temperature are shown in Figure 1.

Given the adopted ambient profiles for these nine species [N_2, O_2, O, O_3, H_2O, H, OH, HO_2, and CO_2], the ambient profiles for all other neutral and charged constituents are determined by solving the photochemical continuity equations under steady state conditions. In doing so, the ambient densities of all species are determined in a self-consistent way. The continuity equations are iterated from an initial guess until the production and loss rates for all species in chemical equilibrium agree to within 1%. The stability of the equilibrium species was then ensured by an additional simulation which verified that their densities changed by no more than 1% during 2h of simulated time. We emphasize that these ambient simulations are performed only to calculate the steady state densities for the species in chemical equilibrium and are not intended to model the full time dynamics of the nighttime mesosphere.

Changes in the number density of the nine neutral species N_2, O_2, O, O_3, H_2O, H, OH, HO_2, and CO_2 due to the electric field heating pulses simulated in this paper were directly calculated and found to be negligible. Changes in odd oxygen and odd hydrogen are primarily driven through changes in atomic oxygen, which is produced during electric field heating predominantly through dissociative reactions R19–R21. For all electric field simulations presented in this paper, percent changes to atomic oxygen were well below 1%. Consequently, the densities of these nine neutral species are taken to be constant during simulations in order to simplify modeling efforts, without introducing any appreciable error on the time scales of interest for this work (tens of seconds or less). Note that all constituents for reactions R157–R162 (used to calculate the ambient ozone profile) are held constant during transient simulations; consequently, reactions R157–R162 are excluded during transient simulations. Additionally, note that for altitudes lower than those simulated in this work (i.e., below 75 km), electric field heating production of atomic oxygen may become significant [e.g., *Sentman et al.*, 2008] due to higher ambient concentrations of O_2 and lower ambient concentrations of atomic oxygen.

2.1. Galactic Cosmic Radiation and Photoionization Processes

The ambient sources of ionization included in this model are galactic cosmic radiation (reactions R1–R7) and photoionization processes due to solar Lyman-β (reaction R8) and Lyman-α (reaction R9) emissions. Ionization due to electron precipitation is negligible outside of the vicinity of the South Atlantic anomaly under normal space weather conditions [*Spjeldvik and Thorne*, 1975; *Abel and Thorne*, 1999] and is thereby excluded in this model.

The parametrization of *Heaps* [1978] is used to calculate the total ion-pair production rate due to galactic cosmic radiation (g.c.r.) for a magnetic latitude of 35° during solar maximum. The branching ratios of g.c.r. interaction with N_2 (reactions R1–R4) are adapted from *Porter et al.* [1976] for proton impact with N_2. The branching ratios for g.c.r. interaction with O_2 (reactions R5–R7) are estimated relative to reactions R1–R4 given the following: (1) the total dissociative cross sections for electron impact of N_2 and O_2 are approximately

equal [*Porter et al.*, 1976]; (2) the total ionization cross sections for electron impact of N_2 and O_2 are approximately equal [*Rapp and Golden*, 1965]; (3) dissociative ionization of N_2 and O_2 accounts for 20% and 30% of the total ionization by electron impact, respectively [*Rapp et al.*, 1965]; and (4) g.c.r. interaction above 30 km is predominately electromagnetic in nature [*Velinov*, 1968; *Heaps*, 1978], so that relationships (1) through (3) listed above for electron interaction may be taken to apply to g.c.r. interaction without serious error.

Solar Lyman-β efficiently ionizes molecular oxygen, and solar Lyman-α efficiently ionizes nitric oxide (see discussion in *Watanabe* [1958]). Both Lyman-β and Lyman-α, emission lines of hydrogen, are efficiently scattered by the Earth's hydrogen geocorona into the nightside ionosphere [e.g., *Thomas*, 1963; *Meier*, 1969; *Young et al.*, 1971]. Nighttime flux of solar Lyman-β have been measured by *Meier* [1969], and nighttime flux of solar Lyman-α have been measured by *Meieir and Mange* [1970, 1973].

For the simulations presented in this paper, the incident flux at 220 km (ϕ_o) for Lyman-β is taken to be 30 R (Rayleigh, 1 R = 10^6 photons cm^{-2} s^{-1}), and for Lyman-α is taken to be 5 kR. These values correspond to solar zenith angles near 120° [*Meier*, 1969; *Meier and Mange*, 1973]. Flux reaching lower altitudes is controlled by photoabsorption via molecular oxygen and is calculated using

$$\phi(z) = \phi_o \, exp\left(- \int_z^{z_o} \sigma \, n \, dz' \right) \tag{1}$$

where σ is the absorption cross section of O_2, n is the density of O_2, z is the altitude, and z_o is the altitude of the incident flux ϕ_o. The absorption cross section of O_2 is taken to be 1.55×10^{-18} cm^2 for Lyman-β and 1.04×10^{-22} cm^2 for Lyman-α [*Watanabe*, 1958].

The ionization rates are calculated by multiplying the solar flux by the ionized species density and its ionization cross section. The ionization cross section of O_2 for Lyman-β is taken to be 0.90×10^{-18} cm^2, and the ionization cross section of NO for Lyman-α is taken to be 2.02×10^{-18} cm^2.

2.2. Electron Attachment, Detachment, and Negative Ion Conversion Processes

The negative ion scheme utilized in this work is largely adopted from *Thomas and Bowman* [1985]. Three-body attachment and three-body detachment processes were calculated from the reaction set of *Sentman et al.* [2008], were found to be negligible at the altitudes modeled in this work (≥75 km), and are thereby excluded. In the following, we discuss why it is necessary to include a nonsimplified negative ion scheme in order to accurately calculate the effect of negative ions on the dynamics of electrons throughout the entire nighttime upper mesosphere.

With the absence of photodetachment during nighttime (see discussion in *Mitra* [1975]), the loss mechanisms for the dominant negative ions [CO_3^-, NO_3^-, HCO_3^-] are as follows: (1) conversion to simpler ions (reaction R69 for CO_3^- and reaction R80 for NO_3^-) and (2) slow ion-ion recombination (reaction R113 for HCO_3^-). Production rates of these dominant negative ions are controlled by the densities of the minor constituents from which they are produced (e.g., reaction R58 for CO_3^-, reactions R78 and R79 for NO_3^-, and reaction R67 for HCO_3^-). In turn, these minor negative ions are sensitive to the reactions which reconvert complex ions into simpler ions (e.g., reactions R51, R56, R62, R68, and R80). Consequently, the negative ion composition in the nighttime upper mesosphere is highly interdependent.

Negative ion dynamics in the upper mesosphere are strongly controlled by atomic oxygen, molecular oxygen, and ozone. Due to the sharp increase in O, decrease in O_2, and general decrease in O_3 with altitude, the negative ion composition undergoes a significant shift throughout the upper mesosphere. The ambient electron and negative ion densities of our simulations are shown in Table 1.

In modeling sprite halos, *Liu* [2012] identified the importance of O^- detachment during electric field heating (as discussed in section 1) and further noted that simplified negative ion schemes may lead to invalid results on time scales greater than several hundreds of milliseconds when the negative ion chemistry is no longer dominated by only a few number of ion species. Our findings are in agreement with those of *Liu* [2012]. Due to the strong interdependence among negative ion species and the diverse negative ion composition exhibited throughout the nighttime upper mesosphere, we found that no simplified negative ion scheme adequately represented the conditions throughout the nighttime upper mesosphere.

Table 1. Ambient Negative Ion Composition (Altitude in km, Densities in cm^{-3})[a]

Altitude	e^-	O^-	O_2^-	O_3^-	O_4^-	OH^-	CO_3^-	CO_4^-	NO_2^-	NO_3^-	$O_2^- \cdot NO$	HCO_3^-	$\sum N_x^+$	λ
75	3.56(−1)	7.35(−2)	7.23	1.12	4.94(−3)	1.07(−2)	1.48(2)	6.25	1.31	1.98(2)	3.94(−4)	5.97(1)	4.22(2)	1.18(3)
76	2.01	4.00(−1)	1.23(1)	6.41(−1)	7.27(−3)	3.94(−2)	8.42(1)	1.22(1)	2.34	8.48(1)	9.46(−4)	1.80(2)	3.79(2)	1.87(2)
77	5.96	7.66(−1)	8.13	1.58(−1)	4.17(−3)	5.24(−2)	2.05(1)	6.07	4.98(−1)	4.02	5.77(−4)	2.38(2)	2.84(2)	4.66(1)
78	1.22(1)	8.75(−1)	3.63	3.12(−2)	1.61(−3)	3.89(−2)	3.94	1.25	3.41(−2)	5.91(−2)	1.48(−4)	1.81(2)	2.03(2)	1.57(1)
79	2.46(1)	8.43(−1)	1.67	7.37(−3)	6.34(−4)	2.03(−2)	8.44(−1)	2.08(−1)	2.44(−3)	9.00(−4)	3.19(−5)	1.05(2)	1.34(2)	4.43
80	4.55(1)	7.53(−1)	9.06(−1)	2.39(−3)	2.96(−4)	7.64(−3)	2.20(−1)	4.02(−2)	2.79(−4)	3.02(−5)	7.85(−6)	4.28(1)	9.02(1)	9.83(−1)

[a] $\sum N_x^+$ is the total positive ion density, and λ is the negative ion to electron ratio. Numbers in ( ) denote factors of ten [e.g, $5.6(-3) = 5.6 \times 10^{-3}$]. Table adapted from *Kotovsky and Moore* [2016].

2.3. Positive Ion Processes

Ionization by g.c.r., photoionization, and electron impact produce the positive ions N^+, N_2^+, O^+, and O_2^+ which quickly convert to NO^+ ions. For the conditions modeled, O_2^+ and NO^+ ions convert into hydronium ion clusters $H_3O^+ \cdot (H_2O)_n$. Clustered positive ions exhibit much higher recombination rate coefficients than simpler positive ions, resulting in significantly decreased ambient electron densities [*Arnold and Krankowsky*, 1978]. Above ~85 km during nighttime, the densities of positive cluster ions drop off rapidly *Mitra* [1975]. For the conditions simulated in this work, positive ions produced during electric field heating convert to hydronium clusters on time scales of seconds to tens of seconds.

The rate coefficients for the conversion of NO^+ ions into hydronium clusters are highly uncertain, involving multiple ion switching reactions with N_2 and CO_2 and highly temperature-dependent collisional dissociative reactions [*Reid*, 1977]. Without sufficient information available to calculate the hydronium ion cluster composition, all water cluster ions are grouped together as one constituent (Y^+). Production of Y^+ proceeds through the initial hydration step of O_2 (reaction R99) and an effective hydration rate for NO^+ (reaction R100). The effective hydration rate for NO^+ is adapted from the empirical study of *Arnold et al.* [1980]. We note that the recombination rate coefficient increases with the hydronium ion cluster order "*n*" [*Johnsen*, 1993]. Without knowledge of the cluster ion composition, we assume a uniform cluster order of $n = 3$, corresponding to a moderately wet and summertime mesosphere [*Reid*, 1977].

2.4. Ion-Ion Recombination

Ion-ion recombination rate coefficients have not been measured between all important ions of the upper mesosphere [*Brasseur and Solomon*, 2005, pp. 576]. Measured reaction rate coefficients and their temperature dependencies for a number of important ion pairs have been measured and agree with theoretical estimates [*Smith and Church*, 1976; *Smith et al.*, 1976; *Smith and Church*, 1977]. Recombination rate coefficients between simple negative ions and clustered positive ions have been found to be comparable with recombination rate coefficients between simple negative ions and simple positive ions. Consequently, we adopt the generalized ion-ion recombination rate coefficient (reaction R113) presented by *Smith and Church* [1977]. Three-body ion-ion processes, important below 30 km [*Smith and Church*, 1977], are excluded.

2.5. Electron Impact Processes

In general, cross sections for a number of electron impact processes (including ionization, attachment, detachment, and recombination) are a function of electron energy [e.g., *Rapp et al.*, 1965; *Rapp and Golden*, 1965; *Rapp and Briglia*, 1965; *Rayment and Moruzzi*, 1978; *Peterson et al.*, 1998; *Brasseur and Solomon*, 2005]. Consequently, the total reaction rate of a given electron impact process involves an integration over the electron energy distribution times the relevant cross section [e.g., see *Brasseur and Solomon*, 2005, Section 2.4.1]. However, for use in models that are not fully kinetic (i.e., models that do not calculate the full electron energy distribution), electron impact reaction rate coefficients are often reported in terms of the mean electron temperature of a Maxwellian distribution or in terms of a reduced electric field producing a steady state electron energy distribution [e.g., *Dulaney et al.*, 1987; *Davies*, 1983; *Kossyi et al.*, 1992]. In our model, the full electron energy distribution is not calculated, and electron impact rate coefficients are updated in terms of either the mean electron temperature or the reduced electric field.

The method for electric field heating utilized in this paper is adapted from *Sentman et al.* [2008]. At the beginning of each simulation, an electric field is applied at altitude with a Gaussian waveshape described by

$E(t) = E_o\ exp(-t^2/\Delta t^2\ )$, where E_o is the peak electric field, and Δt is the "1/e" half width. For the simulations presented in this paper, $2\Delta t = 1$ ms and E_o varies from $\sim 1E_k$ to $\sim 1.3E_k$, where E_k is the conventional breakdown field, taken here to be $[M] \times 123$ Td (Townsend) ($[M]$ is the total gas density (cm^{-3}), and 1 Td$=10^{-17}$ V cm^2). E_k is the minimum electric field (for a given gas density) where ionization rates exceed attachment rates.

The mean electron temperature, T_e (eV), is then determined from the piecewise model of *Sentman et al.* [2008] (two-term spherical harmonic approximation of the Boltzmann equation),

$$3/2\ T_e = \begin{cases} 2.31 \times 10^{-2}\ \theta & \theta < 65\ \text{Td} \\ 3\ (\theta/65)^{2.6}/\ \left[1 + (\theta/65)^2\right] & \theta > 65\ \text{Td} \end{cases}$$

where $\theta = E/[M]$ is the reduced electric field (in units of Townsend, Td). The minimum electron temperature is set to the neutral temperature. Conversion of electron temperature to units of degrees Kelvin can be performed by dividing by the Boltzmann constant, $k = 8.617 \times 10^{-5}$ eVK^{-1}.

When a wave's electric fields are large enough to heat and/or ionize the lower ionosphere, the wave and the plasma mutually interact in a process known as "wave self-action." Consequently, the Gaussian-shaped electric field pulse imposed at individual altitudes in our zero-dimensional simulations are representative of in situ electric fields that would be present after self-action has been accounted for. Additionally, within the ionosphere there is a finite amount of time required for electron temperatures to change in response to electric field heating [e.g., *Gurevich*, 1978, Sections 2.12 and 2.3]. For the conditions modeled, electron temperature relaxation times are on the order of 1 ms or less. In our simulations, the electron temperature is calculated as a function of the instantaneous electric field. Consequently, our application of a Gaussian-shaped electric field pulse can be alternatively viewed as imposing a specific, time-varying electron temperature (which would presumably result from a different in situ electric field waveform). We prefer the later viewpoint, as we feel it more accurately represents the plasma kinetics within the lower ionosphere. However, throughout this work we will cite the values of the modeled electric field (as opposed to the mean electron temperature) in order to enable a more expedient comparison with past literature.

We note that the use of a Gaussian-shaped electric field heating pulse is not meant to replicate lightning electric fields. Rather than attempting to recreate the exact time dynamics of electron and ion changes in response to a precise lightning electric field change, the goal of this paper is meant to highlight more generally the important chemistry processes at play during electric field heating. Regardless, the magnitudes and time durations of the modeled electron temperature enhancements (up to 3 eV with pulse widths of 1 ms) are consistent with those following powerful lightning discharges which produce sprite halos [e.g., *Miyasato et al.*, 2003; *Pasko et al.*, 1997; *Liu*, 2012].

2.6. Numerical Methodology

Heating simulations consist of model runs where an electric field pulse (i.e., electron temperature profile) is applied at the beginning of the model run as described in section 2.5 above. Heating simulations are run independently at a given altitude in the range of 75 and 80 km (this region is chosen as it covers the altitude where significant VLF scattering is expected to occur). At each time step, varying from 10 ns during heating to 100 μs following heating, reaction rate coefficients are updated as a function of the electron temperature or reduced electric field. Subsequently, the densities of the 29 dynamic species are simultaneously updated by solving the photochemical continuity equations (see section 2.1 above) using a first-order accurate forward finite difference scheme. Time steps (δt) were chosen to ensure that the time evolution of each species is stable (i.e., $\frac{\mathrm{d}}{\mathrm{d}t}[n_i]\delta t \ll [n_i]$).

We consider the electron plasma heating to be over when (1) electron impact rates, increased with electron temperature, are negligible, and (2) the rate coefficients of electric field enhanced attachment and detachment processes are near their ambient values. For the conditions modeled in this paper, heating is considered over when the electron temperatures are on the order of a few hundred meV or less (for $2\Delta t = 1$ ms, heating is approximately over after $t = 1$ ms).

Separate nonheating simulations were also run whereby an electron and ion enhancement was imposed at time $t = 0$, after which ambient temperature dynamics were modeled via the photochemical continuity equations using a time step that ranged from 1 to 100 μs. Details regarding the exact electron and ion enhancements modeled are given below where the simulations are described more fully.

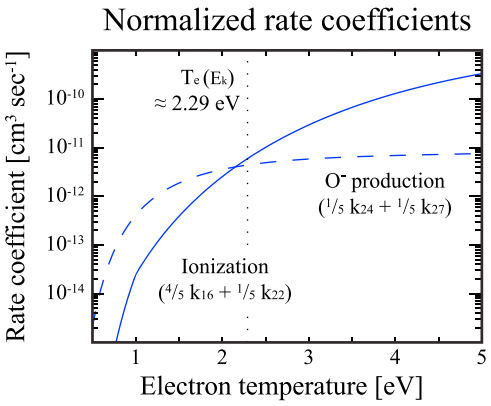

Figure 2. Rate coefficients for ionization (solid trace) and the production of O^- (dashed trace) as a function of electron temperature. Vertical dotted line is shown at 2.29 eV, the modeled electron temperature for conventional breakdown field, $E_k/[M] \simeq 123$ Td (Townsend). Coefficients are normalized for a gas mixture of four parts N_2 and one part O_2.

For the time scales of interest to this paper (milliseconds to tens of seconds), the predominant sources of error come from (1) the inaccuracies in the reaction rate coefficients adopted from past work and (2) the grouping of positive ion clusters, Y^+. For the conditions simulated, positive ions produced during electric field heating cluster within ~10 s at 75 km and within ~100 s at 80 km. Inaccuracies in the electron-ion recombination rate due to the grouping of positive ion clusters are present in our model runs only after detachment and attachment processes balance (i.e., after the electron density growth phase), as attachment rates greatly exceed recombination rates for the conditions modeled. Diffusion time scales in the lower ionosphere are much longer than tens of seconds [e.g., *Whitten and Poppoff*, 1965; *Strobel et al.*, 1970; *Frederick and Orsini*, 1982; *Sentman et al.*, 2008].

3. Results

During electric field heating, O^- ions are produced by heterolytic bond cleavage of molecular oxygen, (reaction R24) $e^- + O_2 \rightarrow e^- + O^- + O^+$, and by dissociative attachment of electrons with molecular oxygen, (reaction R27) $e^- + O_2 \rightarrow O^- + O$ (see Appendix A for the reaction set). For all conditions modeled, reaction R27 is the dominant electron loss process—and, consequently, the dominant negative ion production process—during electric field heating. In Figure 2, the rate coefficients of the dominant ionization processes (reactions R16 and R22, electron impact ionization of molecular nitrogen and oxygen, respectively) and the rate coefficients of O^- production (reactions R24 and R27) are shown as a function of electron temperature. Also shown is a vertical dotted line at 2.29 eV, the electron temperature corresponding to E_k. The rate coefficients are normalized for a gas mixture of four parts N_2 and one part O_2. Below an electron temperature of ~2.15 eV, O^- production rates are greater than ionization rates.

After heating has ended, O^- ions are lost through detachment processes, producing electrons (primarily reaction R33, $O^- + O_2 \rightarrow O_3 + e^-$, and reaction R35, $O^- + O \rightarrow O_2 + e^-$), and through charge exchange processes, producing other negative ions (primarily reaction R45, $O^- + O_2 + M \rightarrow O_3^- + M$, and reaction R46, $O^- + O_3 \rightarrow O_3^- + O$). Ion-ion recombination loss of O^- is negligible. Lifetimes of O^- against detachment and charge exchange as a function of altitude for the conditions modeled are shown in Figure 3. Detachment lifetimes initially increase with altitude up to ~77 km due to decreasing air pressure (affecting reaction R33), above which detachment lifetimes decrease due to the sharp increase in nighttime atomic oxygen (affecting reaction R35). Charge exchange lifetimes overall increase with altitude due to decreasing atmospheric pressure and the local minimum in ozone density around 80 km. At ~74 km, an equal amount of O^- ions is lost between charge exchange and detachment. With increasing altitude, more O^- ions are lost by detachment, providing a source of electrons and effectively recycling electrons that were lost by attachment during electric field heating.

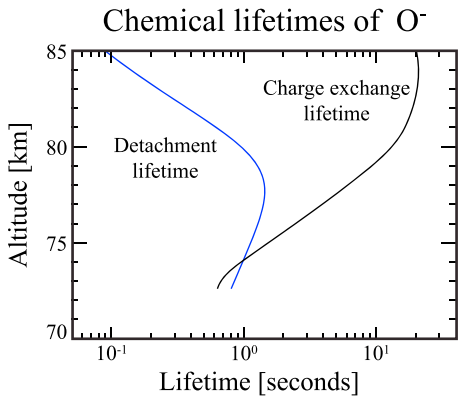

Figure 3. Lifetimes of O^- against detachment and charge exchange as a function of altitude.

If enough O^- are produced during heating, electron detachment from O^- (reactions R33 and R35) after electric field heating can exceed electron loss (primarily reaction R29, $e^- + O_3 \rightarrow O_2^- + O$, and/or electron-ion recombination), leading to a continuous increase in electron density after electric field heating has ended. To demonstrate the importance of O^- detachment following electric field heating, we performed two series of simulations where the electron density, $[e^-]_{enh}$, and

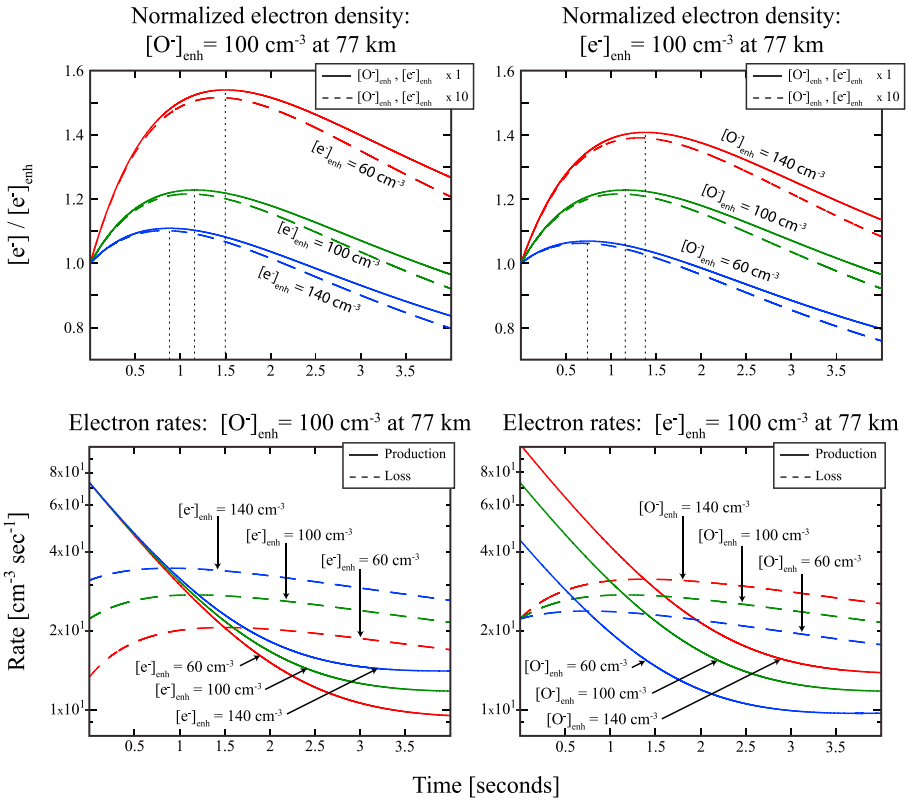

Figure 4. (top row) Normalized electron density dynamics at 77 km for various enhanced densities $[O^-]_{enh}$ and $[e^-]_{enh}$. Solid traces correspond to simulations with enhanced densities at the written value, and dashed traces correspond to initial densities (both O^- and e^-) at 10 times the written value. (bottom row) Corresponding electron production rates (solid traces) and loss rates (dashed traces) for enhanced densities at the written value. (left column) Constant $[O^-]_{enh}$. (right column) Constant $[e^-]_{enh}$.

the O^- density, $[O^-]_{enh}$, were set to enhanced values (larger than their ambient values) at the beginning of the simulations. The density of O_2^+ is also enhanced in order to maintain charge neutrality, as N_2^+, N^+, and O^+ produced during electric field heating are quickly converted to O_2^+. After the enhanced density values are set, the relaxation back toward ambient conditions is modeled. The values of $[e^-]_{enh}$ and $[O^-]_{enh}$ are chosen based upon the results of electric field heating simulations (discussed later) and are representative of e^- and O^- density enhancements immediately following electric field heating which persists near the breakdown potential for relatively long time durations (order of milliseconds).

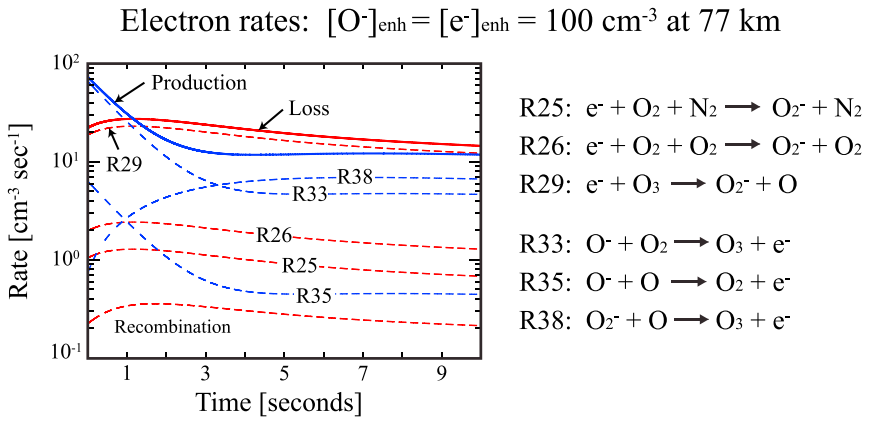

Figure 5. Electron reaction rates at 77 km for $[O^-]_{enh} = [e^-]_{enh} = 100\ cm^{-3}$. All reaction rates not shown are smaller than $10^{-1}\ cm^{-3}\ s^{-1}$.

In the first series of simulations, $[O^-]_{enh}$ is held fixed at 100 cm^{-3}, while $[e^-]_{enh}$ is varied from 60 to 140 cm^{-3}. Resulting dynamics of the electron density at 77 km are shown with solid traces in Figure 4 (top, left). Electron densities shown are normalized by the initial electron density enhancement, so that the variations in risetime and magnitude are readily apparent. Vertical dotted lines are included for each trace, indicating the time of the maximum electron density. As $[e^-]_{enh}$ decreases, both the risetime and magnitude of the electron density enhancement increase. The reasons are best explained by considering the corresponding electron loss and production rates, shown in Figure 4 (bottom, left). A more detailed plot of the electron rates, including individual reaction rates, is shown in Figure 5 for the case $[O^-]_{enh} = [e^-]_{enh} = 100$ cm^{-3}. With increasing $[e^-]_{enh}$, loss rates via attachment (reaction R29, $e^- + O_3 \rightarrow O_2^- + O$; reaction R25, $e^- + O_2 + N_2 \rightarrow O_2^- + N_2$; and reaction R26, $e^- + O_2 + O_2 \rightarrow O_2^- + O_2$) increase. Detachment rates increase slightly with increasing $[e^-]_{enh}$ due to additional detachment from O_2^- (via reaction R38, $O_2^- + O \rightarrow O_3 + e$) produced by electron attachment. For decreasing $[e^-]_{enh}$ given a fixed $[O^-]_{enh}$, the times required for electron loss rates to overtake detachment rates are longer, and the total production rates of electrons are larger — the result is longer risetimes and larger rise magnitudes of the modeled electron density.

In the second series of simulations, $[O^-]_{enh}$ is varied from 60 to 140 cm^{-3}, while $[e^-]_{enh}$ is held fixed at 100 cm^{-3}. The resulting electron density dynamics at 77 km are shown with solid traces in Figure 4 (top, right). Shown in Figure 4 (bottom, right) are the corresponding electron production and loss rates. With increasing $[O^-]_{enh}$, detachment rates of O^- (reactions R33 and R35) increase, leading to increased electron production rates. Due to the additional electron detachment with increasing $[O^-]_{enh}$, electron attachment rates also increase, though less rapidly than electron detachment rates. As a result, for increasing $[O^-]_{enh}$ given a fixed $[e^-]_{enh}$, the modeled electron density enhancements exhibit longer risetimes and larger rise magnitudes.

Additional simulations were run with an order of magnitude increase of the enhanced densities $[O^-]_{enh}$ and $[e^-]_{enh}$. For the first series, $[O^-]_{enh}$ is held fixed at 1000 cm^{-3}, while $[e^-]_{enh}$ is varied from 600 to 1400 cm^{-3}; for the second series, $[O^-]_{enh}$ is varied from 600 to 1400 cm^{-3}, while $[e^-]_{enh}$ is held fixed at 1000 cm^{-3}. The resulting electron densities at 77 km are shown as the dashed traces in Figure 4 (top row). Differences in electron density risetime and magnitude due to the increase in both $[O^-]_{enh}$ and $[e^-]_{enh}$ are attributable to the influence of electron-ion recombination loss. Whereas electron attachment rates are linearly proportional to the electron density, recombination rates are proportional to $(1+\lambda)[e^-]^2$, where λ is the ratio of negative ions to electrons. As a result, recombination rates increase more quickly with $[e^-]_{enh}$ than attachment rates. For large $[e^-]_{enh}$, additional electron loss due to recombination can significantly decrease electron density risetimes. At higher altitudes, where attachment rates decrease due to lower air pressure, electron loss by ion recombination becomes more important, and the electron density risetime dependence on $[e^-]_{enh}$ can be significant. For example, with a tenfold increase of $[O^-]_{enh} = [e^-]_{enh} = 100$ cm^{-3} to $[O^-]_{enh} = [e^-]_{enh} = 1000$ cm^{-3}, additional electron loss by recombination reduces the modeled electron density risetime at 80 km from ~8.0 s to ~4.4 s. In contrast, that same tenfold increase of $[O^-]_{enh}$ and $[e^-]_{enh}$ at 77 km only reduces the modeled electron density risetime by 60 ms from ~1.16 s to ~1.10 s (a difference still measurable by VLF systems).

The waveshape of the electric field change at ionospheric altitudes critically affects the electron density risetime and rise magnitude. The electric field waveform directly affects the time dynamic electron temperature, which drives the production rates of O^- and e^- (see Figure 2). As demonstrated above, the amounts of O^- and e^- produced during electric field heating determine the electron production and loss rates following heating, thereby determining the postheating electron density risetime and magnitude. To demonstrate this, electric field heating at 77 km was simulated for Gaussian-shaped electric field waveforms. Separate simulations were run with different pulse magnitudes, E_o, corresponding to reduced electric field values that vary from 120 to 160 Td. All simulated electric field pulses had widths $2\Delta t = 1$ ms.

In order to highlight the growth of electron densities after electric field heating has ended, the results shown in Figure 6 are normalized by the electron densities ($[e^-]_{1ms}$) immediately following electric field heating (approximately $t = 1$ ms). As discussed above, the importance of O^- detachment depends upon the relative concentrations of electrons and O^-. We have thereby included in Figure 6 the values of $[O^-]$ and $[e^-]$ shortly after electric field heating has ended (after $t = 1$ ms).

Given that all simulated pulses had the same time width ($2\Delta t = 1$ ms), pulses with larger peak magnitudes result in a greater amount of electron production relative to O^- production. As the O^- density decreases relative to the electron density, detachment rates (i.e., electron production rates) reduce relative to electron attachment and electron-ion recombination rates (i.e., electron loss rates), resulting in shorter electron density

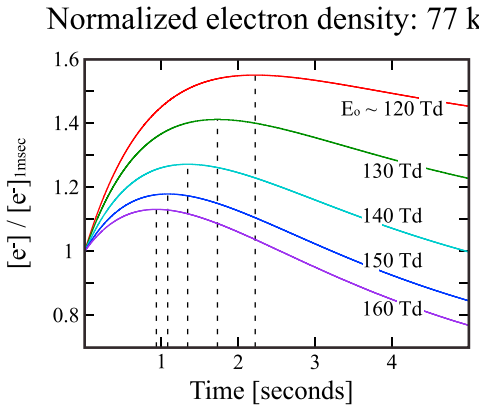

$[O^-]_{1msec}$ / $[e^-]_{1msec}$
Units of cm^{-3}

120 Td:	6.8	/ 5.6	≈ 1.21
130 Td:	10.4	/ 9.1	≈ 1.14
140 Td:	20.3	/ 20.2	≈ 1.01
150 Td:	57.8	/ 66.3	≈ 0.87
160 Td:	269	/ 345	≈ 0.78

Figure 6. Normalized electron densities at 77 km for electric field heating for varying E_o. Electron densities are normalized to $[e^-]$ at 1 ms. $[O^-]$, $[e^-]$, and their ratio at 1 ms for each run are shown on the right.

risetimes and magnitudes. When the relative O^- density produced by electric field heating is small enough (i.e., for high electron temperature heating), postheating electron loss rates will exceed detachment rates and there will be no postheating electron density growth.

The oxygen composition changes with altitude in the nighttime upper mesosphere, directly impacting O^- detachment and e^- attachment rates. With increasing altitude in the nighttime upper mesosphere up until the local ozone minimum around 80 km, ozone densities decrease more rapidly than O_2 densities. As a result, the dominant electron attachment rate (reaction R29, $e^- + O_3 \rightarrow O_2^- + O$) decreases more rapidly with increasing altitude than the dominant O^- detachment rates (reaction R33, $O^- + O_2 \rightarrow O_3 + e^-$, and reaction R35, $O^- + O \rightarrow O_2 + e^-$). Associative detachment of O^- with atomic oxygen (reaction R35) increases with altitude due to the sharp increase in atomic oxygen, largely offsetting the decrease in reaction R33 and eventually increasing the total O^- detachment rate above ~78 km (for the conditions modeled; see Figure 2). Additionally, fewer O^- ions are lost by charge exchange with increasing altitude (see Figure 2), meaning that more O^- will be available for detachment. Consequently, the strength of O^- detachment increases relative to electron attachment with increasing altitude (all else being equal).

The effect of atmospheric composition on electron density risetimes and magnitudes is demonstrated in Figure 7, which shows the results of heating simulations run independently for altitudes varying from 75 to 80 km. At each altitude, the input electric field pulse had a width $2\Delta t = 1$ ms and a reduced peak field $E_o/[M] = 154$ Td. Electron and O^- densities shortly following heating (~1 ms) are also displayed in Figure 7.

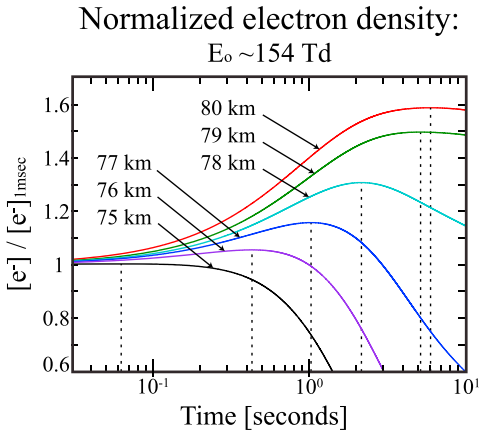

$[O^-]_{1msec}$ / $[e^-]_{1msec}$
Units of cm^{-3}

80 km:	199	/ 296	≈ 0.67
79 km:	160	/ 221	≈ 0.72
78 km:	124	/ 160	≈ 0.78
77 km:	100	/ 121	≈ 0.83
76 km:	60.2	/ 68.4	≈ 0.88
75 km:	20.2	/ 21.5	≈ 0.94

Figure 7. Normalized electron densities at various altitudes for electric field heating with E_o corresponding to 154 Td. Electron densities are normalized to $[e^-]$ at 1 ms. $[O^-]$, $[e^-]$, and their ratio at 1 ms for each run are shown on the right.

With increasing altitude, the decrease in attachment rates—in addition to the increasing percentage of O^- lost via detachment—results in increasing modeled electron density risetimes and magnitudes. At 75 km, the modeled risetime is ~60 ms and the modeled rise magnitude is <1% of $[e^-]_{1ms}$. In contrast, at 80 km, the modeled risetime is ~5.9 s and the modeled rise magnitude is ~58% of $[e^-]_{1ms}$.

4. Discussion

Electric field heating of the upper mesosphere produces O^- ions through heterolytic bond cleavage and dissociative attachment of molecular oxygen. When the density of O^- is large, negative ion detachment rates following electric field heating can exceed electron loss rates (controlled by attachment and/or electron-ion recombination), resulting in continuous growth of the electron density enhancement. Risetimes of modeled electron density enhancements are capable of explaining both <20 ms (i.e., fast) and >20 ms (including slow) onset durations of early VLF scattering events.

The total risetime of electron density enhancements will be controlled by the duration of increased electron temperature (i.e., duration of the electric field change at altitude) and by the dynamics of O^- detachment following electric field heating. A variety of lightning processes—such as continuing currents, *M* components, and subsequent strokes/discharges—can extend the duration of electron temperature heating and thereby electron production. As shown by *Liu* [2012], even electric field changes (i.e., electron temperatures) at subbreakdown values can result in net electron production. *Li et al.* [2012] have shown that the time scales of the lightning charge moment change affect the time dynamics of sprite development. Though sprite halos are typically observed with fast optical durations on the order of milliseconds [e.g., *Stenbaek-Nielsen et al.*, 2000; *Barrington-Leigh et al.*, 2001; *Miyasato et al.*, 2002; *Moudry et al.*, 2003; *Williams et al.*, 2012], sprite elements have been observed with optical durations of up to 100 ms [*Stenbaek-Nielsen and McHarg*, 2008]. Additionally, sprite elements are often observed to be time delayed with respect to their causative lightning return stroke—typical delay times can be a few tens of milliseconds [e.g., *Lyons*, 1996; *São Sabbas et al.*, 2003] but can be as long as ~200 ms [*van der Velde et al.*, 2006]. As shown by *Lu et al.* [2013], time delays and lateral displacements of sprite elements—and thereby time dynamics of ionospheric electric field heating—can be explained by charge removing in-cloud processes associated with continuing currents and *M* components.

In this context, early/fast VLF events can be explained by short-duration (<20 ms) heating without sufficient O^- detachment to produce continuous electron density enhancements beyond heating. Early events exhibiting onset durations >20 ms—ranging from shorter ~100 ms time scales to longer, ≥500 ms time scales of early/slow events—can be explained by sustained ionospheric heating and/or O^- detachment following heating. Additionally, sustained ionospheric heating and/or O^- detachment are capable of explaining early/fast VLF events exhibiting "overshoots," where the scattered field magnitude continues to rise after a sharp initial increase [e.g., *Cotts and Inan*, 2007, Figure 3, event F; *Kotovsky and Moore*, 2015, Figure 3, event C].

Risetimes and magnitudes of electron density enhancements are anticipated to vary spatially within a given ionospheric disturbance, due to spatial variation of both electric field heating and local atmospheric composition. Electric field waveforms reaching ionospheric altitudes will be strongly influenced by ionospheric charge relaxation and wave self-action [e.g., *Pasko et al.*, 1997, Section 3.10; *Gurevich*, 1978, Sections 3.1 and 3.2]. Local atmospheric composition—especially of the oxygen constituents O, O_2, and O_3—strongly affects the relative strengths of electron attachment, O^- detachment, and O^- charge exchange processes. Generally, the significance of O^- detachment increases with altitude, due to the increasing density of atomic oxygen and the overall decreasing densities of ozone (typically exhibiting a local minimum around 80 km) and molecular oxygen.

The observed VLF scattering on ground results from the combined scattering from the entire ionospheric disturbance. If only certain regions of the ionospheric disturbance dominate the total VLF scattering, onset durations might only reflect the risetimes of the electron density enhancement of that specific region. Additionally, the magnitude of VLF scattering is not anticipated to be directly proportional to the magnitude of either the electron density or the plasma conductivity. As a result, the onset dynamics of VLF scattering are not expected to exactly follow the rise dynamics of the electron density enhancement.

For example, if the initial electron density enhancement during heating is large, subsequent electron density growth due either to sustained heating or O^- detachment may not contribute significantly to additional VLF scattering.

Appendix A

Chemical reaction set utilized in this work (Table A1), adapted from *Kotovsky and Moore* [2016]. Integers in parentheses indicate factors of ten—e.g., $5.6(-3) = 5.6 \times 10^{-3}$.

Table A1. Chemical Reaction Set

Reaction No.		Rate Coefficient[a]	Reference(s)[b]
Cosmic ray and photoionization			
R1	$N_2 \xrightarrow[\text{g.c.r.}]{} N_2^+ + e$	$k_1 = 0.8 \times [1.74 \times 10^{-18} + 1.93 \times 10^{-17} \sin^4(35°)]$	[1] [2] [3] [4]
R2	$N_2 \xrightarrow[\text{g.c.r.}]{} N^+ + e + ...$	$k_2 = 0.2 \times [1.74 \times 10^{-18} + 1.93 \times 10^{-17} \sin^4(35°)]$	[1] [2] [3] [4]
R3	$N_2 \xrightarrow[\text{g.c.r.}]{} N + ...$	$k_3 = 0.67 \times [1.74 \times 10^{-18} + 1.93 \times 10^{-17} \sin^4(35°)]$	[1] [2] [3] [4]
R4	$N_2 \xrightarrow[\text{g.c.r.}]{} N^* + ...$	$k_4 = 0.63 \times [1.74 \times 10^{-18} + 1.93 \times 10^{-17} \sin^4(35°)]$	[1] [2] [3] [4]
R5	$O_2 \xrightarrow[\text{g.c.r.}]{} O_2^+ + e$	$k_5 = 0.7 \times [1.74 \times 10^{-18} + 1.93 \times 10^{-17} \sin^4(35°)]$	[1] [2] [3] [4]
R6	$O_2 \xrightarrow[\text{g.c.r.}]{} O^+ + e + ...$	$k_6 = 0.3 \times [1.74 \times 10^{-18} + 1.93 \times 10^{-17} \sin^4(35°)]$	[1] [2] [3] [4]
R7	$O_2 \xrightarrow[\text{g.c.r.}]{} O + ...$	$k_7 = 1.2 \times [1.74 \times 10^{-18} + 1.93 \times 10^{-17} \sin^4(35°)]$	[1] [2] [3] [4]
R8	$O_2 + h\nu(1025.7\text{Å}) \rightarrow O_2^+ + e$	see text	[5] [6] [7]
R9	$NO + h\nu(1215.6\text{Å}) \rightarrow NO^+ + e$	see text	[5] [6] [8]
Electron impact excitation, dissociation, and ionization			
R10	$e^* + N_2 \rightarrow e + N_2(A)$	$\log k_{10} = -(8.4 + 140/\theta)$	[9]
R11	$e^* + N_2 \rightarrow e + N_2(B, W^3, B')$	$k_{11} = k_B = +k_{W^3} + k_{B'}$	[9]
	$N_2(W^3, B') \rightarrow N_2(B)$	$\log k_B = -(8.2 + 148/\theta)$	
		$\log k_{W^3} = -(8.3 + 154/\theta)$	
		$\log k_{B'} = -(8.7 + 168/\theta)$	
R12	$e^* + N_2 \rightarrow e + N_2(a', a, w^1)$	$k_{12} = k_{a'} + k_a + k_{w^1}$	[9]
	$N_2(a, w^1) \rightarrow N_2(a')$	$\log k_{a'} = -(8.8 + 167/\theta)$	
		$\log k_a = -(8.5 + 174/\theta)$	
		$\log k_{w^1} = -(8.7 + 175/\theta)$	
R13	$e^* + N_2 \rightarrow e + N_2(C, E, a'')$	$k_{13} = k_C + k_E + k_{a''}$	[9]
	$N_2(E, a'') \rightarrow N_2(C)$	$\log k_C = -(8.2 + 211/\theta)$	
		$\log k_E = -(10.1 + 254/\theta)$	
		$\log k_{a''} = -(9.2 + 262/\theta)$	
R14	$e^* + N_2 \rightarrow e + N + N$	$k_{14} = 2\,k_{15}$	[10]
		$= 0$, for $\theta < 76$ Td	[9]
R15	$e^* + N_2 \rightarrow e + N + N(^2D)$	$k_{15} = 1(-10)\,[3.096 - 6.71\ (-2)\ \theta\ ...$	[10]
		$+ 3(-4)\ \theta^2 + 1.59(-6)\ \theta^3 - 1.57(-9)\ \ \theta^4]$	
		$= 0$, for $\theta < 76$ Td	[9]
R16	$e^* + N_2 \rightarrow e + e + N_2^+$	$\log k_{16} = -(8.3 + 365/\theta)$	[9]
R17	$e^* + O_2 \rightarrow e + O_2(a^1\Delta_g)$	$\log k_{17} = -(9 + 52/\theta)$, for $\theta < 40$	[9]
		$= -(10.2 + 3.5/\theta)$, for $\theta > 40$	
R18	$e^* + O_2 \rightarrow e + O_2(b)$	$\log k_{18} = -(9.5 + 60/\theta)$, for $\theta < 30$	[9]
		$= -(11.2 + 7.2/\theta)$, for $\theta > 30$	
R19	$e^* + O_2 \rightarrow e + O + O$	$\log k_{19} = -(7.9 + 134/\theta)$	[9]
R20	$e^* + O_2 \rightarrow e + O + O(^1D)$	$\log k_{20} = -(8 + 169/\theta)$	[9]
R21	$e^* + O_2 \rightarrow e + O + O(^1S)$	$\log k_{21} = -(8.8 + 119/\theta)$	[9]

Table A1. (continued)

Reaction No.		Rate Coefficient[a]	Reference(s)[b]
R22	$e^* + O_2 \rightarrow e + e + O_2^+$	$\log k_{22} = -(8.8 + 281/\theta)$	[9]
R23	$e^* + O_2 \rightarrow e + e + O^+ + O$	$k_{23} = 3.18(-14)\ (T_e/300)\ \exp(-206055/T_e)$	[10]
R24[c]	$e^* + O_2 \rightarrow e + O^- + O^+$	$k_{24} = 7.10(-11)\ T_e^{0.5}\ \exp(-17/T_e)$	[11]
Electron attachment			
R25	$e + O_2 + N_2 \rightarrow O_2^- + N_2$	$k_{25} = 1.07(-31)\ (300/T_e)^2\ \exp(-70/T_e)$ $\times \exp\left[1500(T_e - T_n)/(T_e\ T_n)\right]$	[9]
R26	$e + O_2 + O_2 \rightarrow O_2^- + O_2$	$k_{26} = 1.4(-29)\ (300/T_e)\ \exp(-600/T_e)$ $\times \exp\left[700(T_e - T_n)/(T_e\ T_n)\right]$	[9]
R27[c]	$e^* + O_2 \rightarrow O^- + O$	$k_{27} = 1.07(-9)\ T_e^{-1.39}\ \exp(-6.26/T_e)$	[11]
R28[c]	$e + O_3 \rightarrow O^- + O_2$	$k_{28} = 2.12(-9)\ T_e^{-1.06}\ \exp(-0.93/T_e)$	[11]
		$= 1(-11)$, for $T_e < 0.13$ eV	[9]
R29[c]	$e + O_3 \rightarrow O_2^- + O$	$k_{29} = 9.76(-8)\ T_e^{-1.309}\ \exp(-1.007/T_e)$	[11]
		$= 1(-9)$, for $T_e < 0.14$ eV	[9]
Electron detachment			
R30[c]	$O^- + e^* \rightarrow O + e + e$	$k_{30} = 5.47(-8)\ T_e^{0.324}\ \exp(-2.98/T_e)$	[11]
R31	$O^- + N_2 \rightarrow N_2O + e$	$\log k_{31} = a + b\log(\theta) + c\log(\theta)^2$ $a = -15.66,\ b = 2.97,\ c = -0.58$	[12][d]
R32	$O^- + N \rightarrow NO + e$	$k_{32} = 3(-10)$	[9]
R33	$O^- + O_2 \rightarrow O_3 + e$	$k_{33} = 5.00(-15)$	[11]
R34	$O^- + O_2(a^1\Delta_g) \rightarrow O_3 + e$	$k_{34} = 1.42(-10)$	[11]
R35	$O^- + O \rightarrow O_2 + e$	$k_{35} = 2.30(-10)$	[11]
R36	$O^- + NO \rightarrow NO_2 + e$	$k_{36} = 2.6(-10)$	[9]
R37	$O_2^- + O_2(a^1\Delta_g) \rightarrow O_2 + O_2 + e$	$k_{37} = 2.00(-10)$	[11]
R38	$O_2^- + O \rightarrow O_3 + e$	$k_{38} = 3.30(-10)$	[11]
R39	$O_3^- + O \rightarrow O_2 + O_2 + e$	$k_{39} = 1.0(-10)$	[13]
R40	$O_3^- + O_3 \rightarrow O_2 + O_2 + O_2 + e$	$k_{40} = 1.0(-10)$	[13]
R41	$OH^- + O \rightarrow HO_2 + e$	$k_{41} = 2.0(-10)$	[13]
R42	$OH^- + H \rightarrow H_2O + e$	$k_{42} = 1.4(-9)$	[13]
R43	$NO_2^- + O \rightarrow NO_2 + e$	$k_{43} = 1(-12)$	[9]
Negative ion conversion			
R44	$O^- + O_2(a^1\Delta_g) \rightarrow O_2^- + O$	$k_{44} = 4.75(-11)$	[11]
R45	$O^- + O_2 + M \rightarrow O_3^- + M$	$k_{45} = 1.10(-30)\ (300/T_n)$	[9]
R46	$O^- + O_3 \rightarrow O_3^- + O$	$k_{46} = 5.30(-10)$	[11]
R47	$O^- + H_2O \rightarrow OH^- + OH$	$k_{47} = 6.0(-13)$	[13]
R48	$O^- + CO_2 + M \rightarrow CO_3^- + M$	$k_{48} = 2.0(-28)$	[13]
R49	$O^- + NO + M \rightarrow NO_2^- + M$	$k_{49} = 1(-29)$	[9]
R50	$O^- + NO_2 \rightarrow NO_2^- + O$	$k_{50} = 1.0(-9)$	[13]
R51	$O_2^- + O \rightarrow O^- + O_2$	$k_{51} = 3.31(-10)$	[11]
R52	$O_2^- + O_3 \rightarrow O_3^- + O_2$	$k_{52} = 4.00(-11)$	[11]
R53	$O_2^- + O_2 + M \rightarrow O_4^- + M$	$k_{53} = 3.50(-31)\ (300/T_n)$	[9]
R54	$O_2^- + CO_2 + M \rightarrow CO_4^- + M$	$k_{54} = 4.7(-29)$	[13]
R55	$O_2^- + NO_2 \rightarrow NO_2^- + O_2$	$k_{55} = 7.0(-10)$	[13]
R56	$O_3^- + O \rightarrow O_2^- + O_2$	$k_{56} = 2.5(-10)$	[13]
R57	$O_3^- + H \rightarrow OH^- + O_2$	$k_{57} = 8.4(-10)$	[13]

Table A1. (continued)

Reaction No.		Rate Coefficient[a]	Reference(s)[b]
R58	$O_3^- + CO_2 \rightarrow CO_3^- + O_2$	$k_{58} = 5.5(-10)$	[13]
R59	$O_3^- + NO \rightarrow NO_3^- + O$	$k_{59} = 2.6(-12)$	[13]
R60	$O_3^- + NO_2 \rightarrow NO_3^- + O_2$	$k_{60} = 2.8(-10)$	[13]
R61	$O_4^- + O_2(a^1\Delta_g) \rightarrow O_2^- + O_2 + O_2$	$k_{61} = 1(-10)$	[9]
R62	$O_4^- + O \rightarrow O_3^- + O_2$	$k_{62} = 4.0(-10)$	[13]
R63	$O_4^- + CO_2 \rightarrow CO_4^- + O_2$	$k_{63} = 4.3(-10)$	[13]
R64	$O_4^- + NO \rightarrow O_2^- \cdot NO + O_2$	$k_{64} = 2.5(-10)$	[13]
R65	$OH^- + O_3 \rightarrow O_3^- + OH$	$k_{65} = 9.0(-10)$	[13]
R66	$OH^- + NO_2 \rightarrow NO_2^- + OH$	$k_{66} = 1.1(-9)$	[13]
R67	$OH^- + CO_2 + M \rightarrow HCO_3^- + M$	$k_{67} = 7.6(-28)$	[13]
R68	$CO_3^- + O \rightarrow O_2^- + CO_2$	$k_{68} = 1.1(-10)$	[13]
R69	$CO_3^- + O_2 \rightarrow O_3^- + CO_2$	$k_{69} = 6.0(-15)$	[13]
R70	$CO_3^- + H \rightarrow OH^- + CO_2$	$k_{70} = 1.7(-10)$	[13]
R71	$CO_3^- + NO_2 \rightarrow NO_2^- + CO_2$	$k_{71} = 1.1(-11)$	[13]
R72	$CO_3^- + NO_2 \rightarrow NO_3^- + CO_2$	$k_{72} = 2.0(-10)$	[13]
R73	$CO_4^- + O_3 \rightarrow O_3^- + O_2 + CO_2$	$k_{73} = 1.3(-10)$	[13]
R74	$CO_4^- + O \rightarrow CO_3^- + O_2$	$k_{74} = 1.4(-10)$	[13]
R75	$CO_4^- + H \rightarrow CO_3^- + OH$	$k_{75} = 2.2(-10)$	[13]
R76	$CO_4^- + NO \rightarrow O_2^- \cdot NO + CO_2$	$k_{76} = 4.8(-11)$	[13]
R77	$NO_2^- + H \rightarrow OH^- + NO$	$k_{77} = 3.0(-10)$	[13]
R78	$NO_2^- + O_3 \rightarrow NO_3^- + O_2$	$k_{78} = 1.2(-10)$	[13]
R79	$NO_2^- + NO_2 \rightarrow NO_3^- + NO$	$k_{79} = 2.0(-13)$	[13]
R80	$NO_3^- + O \rightarrow NO_2^- + O_2$	$k_{80} \leq 1(-11)$	[13]
R81	$NO_3^- + O_3 \rightarrow NO_2^- + O_2 + O_2$	$k_{81} = 1.0(-13)$	[13]
R82	$O_2^- \cdot NO + CO_2 \rightarrow CO_3^- + NO_2$	$k_{82} = 1.0(-11)$	[13]
R83	$O_2^- \cdot NO + NO \rightarrow NO_2^- + NO_2$	$k_{83} = 1.5(-11)$	[13]
R84	$O_2^- \cdot NO + H \rightarrow NO_2^- + OH$	$k_{84} = 7.2(-10)$	[13]
Positive ion conversion			
R85	$N^+ + O_2 \rightarrow O_2^+ + N$	$k_{85} = 2.8(-10)$	[9]
R86	$N^+ + O_2 \rightarrow NO^+ + O$	$k_{86} = 2.5(-10)$	[9]
R87	$N^+ + O_2 \rightarrow O^+ + NO$	$k_{87} = 2.8(-11)$	[9]
R88	$O^+ + N_2 \rightarrow NO^+ + N$	$k_{88} = 3(-12)\ \exp(-3.11\times10^{-3}\ T_n)$	[9]
R89	$O^+ + O_2 \rightarrow O_2^+ + O$	$k_{89} = 3.3(-11)\ \exp(-1.69\times10^{-3}\ T_n)$	[9]
R90	$O^+ + N_2 + M \rightarrow NO^+ + N + M$	$k_{90} = 6(-29)\ (300/T_n)^2$	[9]
R91	$N_2^+ + O_2 \rightarrow O_2^+ + N_2$	$k_{91} = 5.1(-11)\ (T_n/300)^{-0.8}$	[14]
R92	$N_2^+ + O_2 \rightarrow NO^+ + NO$	$k_{92} = 3(-14)$	[15]
R93	$N_2^+ + O \rightarrow NO^+ + N(^2D)$	$k_{93} = 1.4(-10)\ (T_n/300)^{-0.44}$	[14]
R94	$O_2^+ + N_2 \rightarrow NO^+ + NO$	$k_{94} = 1(-15)$	[15]
R95	$O_2^+ + N \rightarrow NO^+ + O$	$k_{95} = 1.8(-10)$	[14]
R96	$O_2^+ + NO \rightarrow NO^+ + O_2$	$k_{96} = 4.4(-10)$	[14]
R97	$O_2^+ + O_2 + M \rightarrow O_4^+ + M$	$k_{97} = 2.6(-30)\ (300/T_n)^{3.2}$	[16]
R98	$O_4^+ + O \rightarrow O_2^+ + O_3$	$k_{98} = 3.0(-10)$	[16]
R99	$O_4^+ + H_2O \rightarrow O_2^+ \cdot (H_2O) + O_2$	$k_{99} = 1.5(-9)$	[16]
R100	$NO^+ + M + M \rightarrow NO^+ \cdot (H_2O) + M$	see text	[17]

Table A1. (continued)

Reaction No.		Rate Coefficient[a]	Reference(s)[b]
Electron-ion recombination			
R101	$N_2^+ + e \rightarrow N(^4S) + N(^2D)$	$k_{101} = 0.37 \times 2.2(-7)\ (300/T_n)^{0.2}\ (T_e/T_n)^{-0.39}$	[18] [19] [20]
R102	$N_2^+ + e \rightarrow N(^2P) + N(^4S)$	$k_{102} = 0.11 \times 2.2(-7)\ (300/T_n)^{0.2}\ (T_e/T_n)^{-0.39}$	[18] [19] [20]
R103	$N_2^+ + e \rightarrow N(^2D) + N(^2D)$	$k_{103} = 0.52 \times 2.2(-7)\ (300/T_n)^{0.2}\ (T_e/T_n)^{-0.39}$	[18] [19] [20]
R104[e]	$NO^+ + e \rightarrow N(^4S) + O(^3P)$	$k_{104} = 0.05 \times 3.5(-7)\ (300/T_n)\ (T_e/T_n)^{-0.69}$	[18] [19] [21]
R105[e]	$NO^+ + e \rightarrow N(^2D) + O(^3P)$	$k_{105} = 0.95 \times 3.5(-7)\ (300/T_n)\ (T_e/T_n)^{-0.69}$	[18] [19] [21]
R106[f]	$NO^+ + e^* \rightarrow N(^4S) + O(^3P)$	$k_{106} = 0.10 \times 3.5(-7)\ (300/T_n)\ (T_e/T_n)^{-0.69}$	[18] [19] [21]
R107[f]	$NO^+ + e^* \rightarrow N(^4S) + O(^1D)$	$k_{107} = 0.10 \times 3.5(-7)\ (300/T_n)\ (T_e/T_n)^{-0.69}$	[18] [19] [21]
R108[f]	$NO^+ + e^* \rightarrow N(^2D) + O(^3P)$	$k_{108} = 0.70 \times 3.5(-7)\ (300/T_n)\ (T_e/T_n)^{-0.69}$	[18] [19] [21]
R109[f]	$NO^+ + e^* \rightarrow N(^2P) + O(^3P)$	$k_{109} = 0.10 \times 3.5(-7)\ (300/T_n)\ (T_e/T_n)^{-0.69}$	[18] [19] [21]
R110	$O_2^+ + e \rightarrow O + O$	$k_{110} = 1.95(-7)\ (300/T_n)^{0.7}\ (T_e/T_n)^{-0.7}$	[18] [19]
R111	$O_4^+ + e \rightarrow O_2 + O_2$	$k_{111} = 4.2(-6)\ (T_e/T_n)^{-0.48}$	[22]
R112	$H_3O^+ \cdot (H_2O)_n + e \rightarrow$ neutrals	$k_{112} = (0.5 + 2n) \times 10^{-6}\ (300/T_e)^{1/2}$	[23] [24]
Ion-ion recombination			
R113	$A^+ + B^- \rightarrow A + B$	$k_{113} = 6(-8)\ (300/T_i)^{1/2}$	[25]
Active-state N_2 chemistry			
R114	$N_2(A) + O_2 \rightarrow N_2 + O_2(a^1\Delta_g)$	$k_{114} = 1.29(-12)$	[9]
R115	$N_2(A) + O_2 \rightarrow N_2 + O_2(b)$	$k_{115} = 1.29(-12)$	[9]
R116	$N_2(A) + O_2 \rightarrow N_2 + O + O$	$k_{116} = 2.54(-12)$	[9]
R117	$N_2(A) + O \rightarrow NO + N(^2D)$	$k_{117} = 7(-12)$	[9]
R118	$N_2(A) + N \rightarrow N_2 + N(^2P)$	$k_{118} = 5(-11)$	[9]
R119	$N_2(B) \rightarrow N_2(A) + h\nu\ (1PN_2)$	$k_{119} = 1.5(5)$	[9]
R120	$N_2(B) + N_2 \rightarrow N_2(A) + N_2$	$k_{120} = 5(-11)$	[9]
R121	$N_2(B) + O_2 \rightarrow N_2 + O + O$	$k_{121} = 3(-10)$	[9]
R122	$N_2(a') + N_2 \rightarrow N_2(B) + N_2$	$k_{122} = 2(-13)$	[9]
R123	$N_2(a') + O_2 \rightarrow N_2 + O + O$	$k_{123} = 2.8(-11)$	[9]
R124	$N_2(a') + NO \rightarrow N_2 + N + O$	$k_{124} = 3.6(-10)$	[9]
R125	$N_2(C) \rightarrow N_2(B) + h\nu\ (2PN_2)$	$k_{125} = 3(7)$	[9]
R126	$N_2(C) + N_2 \rightarrow N_2(a') + N_2$	$k_{126} = 1(-11)$	[9]
R127	$N_2(C) + O_2 \rightarrow N_2 + O + O(^1S)$	$k_{127} = 3(-10)$	[9]
Active-state O_2 chemistry			
R128	$O_2(a^1\Delta_g) \rightarrow O_2 + h\nu\ (O_2$IR Atm)	$k_{128} = 2.6(-4)$	[26]
R129	$O_2(a^1\Delta_g) + N_2 \rightarrow O_2 + N_2$	$k_{129} = 3(-21)$	[9]
R130	$O_2(a^1\Delta_g) + O_2 \rightarrow O_2 + O_2$	$k_{130} = 2.2(-18)\ (T_n/300)^{0.8}$	[9]
R131	$O_2(a^1\Delta_g) + N \rightarrow NO + O$	$k_{131} = 2(-14)\ \exp(-600/T_n)$	[9]
R132	$O_2(a^1\Delta_g) + O \rightarrow O_2 + O$	$k_{132} = 7(-16)$	[9]
R133	$O_2(a^1\Delta_g) + NO \rightarrow O_2 + NO$	$k_{133} = 2.5(-11)$	[9]
R134	$O_2(b) \rightarrow O_2 + h\nu\ (O_2$ Atm)	$k_{134} = 7.7(-2)$	[10]
R135	$O_2(b) + N_2 \rightarrow O_2(a^1\Delta_g) + N_2$	$k_{135} = 4.9(-15)\ \exp(-253/T_n)$	[9]
R136	$O_2(b) + O_2 \rightarrow O_2(a^1\Delta_g) + O_2$	$k_{136} = 4.3(-22)\ T_n^{2.4}\ \exp(-241/T_n)$	[9]
R137	$O_2(b) + O \rightarrow O_2(a^1\Delta_g) + O$	$k_{137} = 8(-14)$	[9]
R138	$O_2(b) + O_3 \rightarrow O_2 + O_2 + O$	$k_{138} = 1.8(-11)$	[9]

Table A1. (continued)

Reaction No.		Rate Coefficient[a]	Reference(s)[b]
Odd nitrogen chemistry			
R139	$N(^4S) + O + M \rightarrow NO + M$	$k_{139} = 6.9(-33)\exp(136/T_n)$	[15]
R140	$N(^4S) + O_3 \rightarrow NO + O_2$	$k_{140} = 3(-11)\exp(-1200/T_n)$	[27]
R141	$N(^4S) + O_2 \rightarrow NO + O$	$k_{141} = 4.4(-12)\exp(-3220/T_n)$	[28]
R142	$N(^2D) + O_2 \rightarrow NO + O$	$k_{142} = 6.0(-12)$	[28]
R143	$N(^4S) + NO \rightarrow N_2 + O$	$k_{143} = 3.4(-11)$	[28]
R144	$N(^2D) + NO \rightarrow N_2 + O$	$k_{144} = 7.0(-11)$	[28]
R145	$NO + O \rightarrow NO_2 + h\nu$	$k_{145} = 4.2(-18)$	[29]
R146	$NO + O + M \rightarrow NO_2 + M\,(+ h\nu)$	$k_{146} = 2.48(-33)\exp(906/T_n)$	[30] [31]
R147	$NO + O_3 \rightarrow NO_2 + O_2\,(+ h\nu)$	$k_{147} = 9.47(-13)\exp(-1238/T_n)$	[32]
R148	$N(^4S) + NO_2 \rightarrow N_2O + O$	$k_{148} = 0.43 \times 1.8(-11)$	[27]
R149	$N(^4S) + NO_2 \rightarrow N_2 + O + O$	$k_{149} = 0.13 \times 1.8(-11)$	[27]
R150	$N(^4S) + NO_2 \rightarrow N_2 + O_2$	$k_{150} = 0.10 \times 1.8(-11)$	[27]
R151	$N(^4S) + NO_2 \rightarrow NO + NO$	$k_{151} = 0.33 \times 1.8(-11)$	[27]
R152	$O + NO_2 \rightarrow NO + O_2$	$k_{152} = 3.2(-11)\exp(-300/T_n)$	[27]
R153	$N(^2D) \rightarrow N(^4S) + h\nu$	$k_{153} = 1.07(-5)$	[28]
R154	$N(^2D) + N_2 \rightarrow N(^4S) + N_2$	$k_{154} = 6(-15)$	[9]
R155	$N(^2D) + O \rightarrow N(^4S) + O$	$k_{155} = 1(-12)$	[28]
Odd oxygen chemistry			
R156	$O + O + M \rightarrow O_2(a^1\Delta_g) + M$	$k_{156} = 0.25 \times 9.59(-34)\exp(480/T_n)$	[26] [33]
R157	$O + O_2 + N_2 \rightarrow O_3 + N_2$	$k_{157} = 8.82(-35)\exp(575/T_n)$	[33]
R158	$O + O_2 + O_2 \rightarrow O_3 + O_2$	$k_{158} = 2.15(-34)\exp(345/T_n)$	[33]
R159	$O + O_3 \rightarrow O_2 + O_2$	$k_{159} = 1.5(-11)\exp(-2218/T_n)$	[33]
R160	$OH + O_3 \rightarrow HO_2 + O_2$	$k_{160} = 1.6(-12)\exp(-940/T_n)$	[33]
R161	$H + O_3 \rightarrow OH + O_2$	$k_{161} = 1.4(-10)\exp(-270/T_n)$	[33]
R162	$HO_2 + O_3 \rightarrow OH + O_2 + O_2$	$k_{162} = 1.4(-14)\exp(-580/T_n)$	[33]

[a]Rate coefficients are in units of s^{-1} for single-body reactions, $cm^3\ s^{-1}$ for two-body reactions, and $cm^6\ s^{-1}$ for three-body reactions.

[b][1] *Heaps* [1978], [2] *Porter et al.* [1976], [3] *Rapp et al.* [1965], [4] *Rapp and Golden* [1965], [5] *Watanabe* [1958], [6] *Strobel and Young* [1974], [7] *Meier* [1969], [8] *Meier and Mange* [1973], [9], *Kossyi et al.* [1992], [10] *Sentman et al.* [2008], [11] *Gudmundsson and Thorsteinsson* [2007], [12] *Rayment and Moruzzi* [1978], [13] *Thomas and Bowman* [1985], [14] *Cleary* [1986], [15] *Ogawa and Shimazaki* [1975], [16] *Brasseur and Solomon* [1986], [17] *Arnold et al.* [1980], [18] *Sheehan and St.-Maurice* [2004], [19] *Biondi* [1975], [20] *Peterson et al.* [1998], [21] *Hellberg et al.* [2003] [22] *Dulaney et al.* [1988], [23] *Johnsen* [1993], [24] *Leu et al.* [1973], [25] *Smith and Church* [1977], [26] *Bowman and Thomas* [1974], [27] *Strobel* [1971], [28] *Barth* [1992] , [29] *Becker et al.* [1973], [30], *Clyne and Thrush* [1962], [31] *Golomb and Brown* [1975], [32] *Clyne et al.* [1964], [33] *Allen et al.* [1984].

[c]T_e are in units of eV.

[d]Derived from Figure 4 of *Rayment and Moruzzi* [1978].

[e]For mean electron energy, $E_e < 1.25$ eV.

[f]For mean electron energy, $E_e > 1.25$ eV.

Acknowledgments
This work is supported by DARPA/US Air Force contract FA8650-15-C-7535 and NSF grant PLR-1246275 to the University of Florida. The authors would like to thank Martin A. Uman for his helpful comments on the manuscript. Data utilized in this paper, including the NRLMSISE-00 neutral constituency and temperature, are available upon request by contacting R. C. Moore (moore@ece.ufl.edu).

References

Abel, B., and R. M. Thorne (1999), Modeling energetic electron precipitation near the South Atlantic anomaly, *J. Geophys. Res.*, *104*(A4), 7037–7044.

Allen, M., J. I. Lunine, and Y. L. Yung (1984), The vertical distribution of ozone in the mesosphere and lower thermosphere, *J. Geophys. Res.*, *89*(D3), 4841–4872.

Arnold, F., and D. Krankowsky (1978), Mid-latitude lower ionosphere structure and composition measurements during winter, *J. Atmos. Terr. Phys.*, *41*, 1127–1140.

Arnold, F., D. Krankowsky, E. Zettwitz, and W. Joos (1980), Strong temperature control of the ionospheric *D*-region: Evidence from in situ ion composition measurements, *J. Atmos. Terr. Phys.*, *42*, 249–256.

Barrington-Leigh, C. P., U. S. Inan, and M. Stanley (2001), Identification of sprites and elves with intensified video and broadband array photometry, *J. Geophys. Res.*, *106*(A2), 1741–1750, doi:10.1029/2000JA000073.

Barth, C. A. (1992), Nitric oxide in the lower thermosphere, *Planet. Space Sci.*, *40*(23), 315–336.
Becker, K. H., W. Groth, and D. Thran (1973), Mechanism of the air afterglow NO + O → NO+ + hν, *Symp. Int. Combust.*, *14*(1), 353–363.
Biondi, M. A. (1975), Charged-particle recombination processes, in *Defense Nuclear Reactions Rate Handbook*. DNA1948H, Revision No. 6.
Boeck, W. L., O. H. Vaughan Jr., R. Blakeslee, B. Vonnegut, and M. Brook (1992), Lightning induced brightening in the airglow layer, *Geophys. Res. Lett.*, *19*(2), 99–102.
Bowman, M. R., and L. Thomas (1974), Numerical studies of oxygen-hydrogen constituents in the mesosphere and thermosphere—Effect of changing chemical rate coefficients, *J. Atmos. Terr. Phys.*, *86*, 657–665.
Brasseur, G. P., and S. Solomon (1986), *Aeronomy of the Middle Atmosphere*, 2nd ed., edited by D. Reidel, Springer, Boston, Mass.
Brasseur, G. P., and S. Solomon (2005), *Aeronomy of the Middle Atmosphere*, 3rd ed., Springer, Dordrecht, Netherlands.
Cleary, D. D. (1986), Daytime high-latitude rocket observations of the NO γ, δ, and ϵ bands, *J. Geophys. Res.*, *91*(A10), 11,337–11,344.
Clyne, M. A. A., and B. A. Thrush (1962), Mechanism of chemiluminescent combination reactions involving oxygen atoms, *Proc. R. Soc. Lond. A.*, *269*, 404–418.
Clyne, M. A. A., B. A. Thrush, and R. P. Wayne (1964), Kinetics of the chemiluminescent reaction between nitric oxide and ozone, *J. Chem. Soc. Faraday Trans.*, *60*, 359–370.
Cotts, B. R. T., and U. S. Inan (2007), VLF observation of long ionospheric recovery events, *Geophys. Res. Lett.*, *34*, L14809, doi:10.1029/2007GL030094.
Davies, D. K. (1983), Measurements of swarm parameters in dry air, in *Theoretical Notes, Note 346*, Westinghouse R & D Center, Pittsburgh, Pa.
Dulaney, J. L., M. A. Biondi, and R. Johnsen (1987), Electron temperature dependence of the recombination of electrons with NO^+ ions, *Phys. Rev. A.*, *36*(3), 1342–1350.
Dulaney, J. L., M. A. Biondi, and R. Johnsen (1988), Electron-temperature dependence of the recombination of electrons with O_4^+ ions, *Phys. Rev. A.*, *37*(7), 2539–2542.
Franz, R. C., R. J. Nemzek, and J. R. Winckler (1990), Television image of a large upward electrical discharge above a thunderstorm system, *Science*, *249*(4964), 48–51.
Frederick, J. E., and N. Orsini (1982), The distribution and variability of mesospheric odd nitrogen: A theoretical investigation, *J. Atmos. Terr. Phys.*, *44*(6), 479–488.
Golomb, D., and J. H. Brown (1975), The temperature dependence of the NO-O chemiluminous recombination. The RMC mechanism, *J. Chem. Phys.*, *63*(12), 5246–5251.
Gudmundsson, J. T., and E. G. Thorsteinsson (2007), Oxygen discharges diluted with argon: Dissociation processes, *Plasma Sources Sci. Technol.*, *16*, 399–412.
Gurevich, A. V. (1978), *Nonlinear Phenomena in the Ionosphere*, translated by J. George Adashko, Springer-Verlag, New York.
Haldoupis, C., T. Neubert, U. S. Inan, A. Mika, T. H. Allin, and R. A. Marshall (2004), Subionospheric early VLF signal perturbations observed in one-to-one association with sprites, *J. Geophys. Res.*, *109*, A10303, doi:10.1029/2004JA010651.
Haldoupis, C., R. J. Steiner, A. Mika, S. Shalimov, R. A. Marshall, U. S. Inan, T. Bosinger, and T. Neubert (2006), "Early/slow" events: A new category of VLF perturbations observed in relation with sprites, *J. Geophys. Res.*, *111*, A11321, doi:10.1029/2006JA011960.
Heaps, M. G. (1978), Parametrization of the cosmic ray ion-pair production rate above 18 km, *Planet. Space Sci.*, *26*, 513–517.
Hellberg, F., S. Rosén, R. Thomas, A. Neau, M. Larsson, A. Petrignani, and W. J. van der Zande (2003), Dissociative recombination of NO^+: Dynamics of the X $1\Sigma^+$ and a $3\Sigma^+$ electronic states, *J. Chem. Phys.*, *118*(14), 6250–6259.
Inan, U. S., D. C. Shafer, W. Y. Yip, and R. E. Orville (1988), Subionospheric VLF signatures of nighttime *D*-region perturbations in the vicinity of lightning discharges, *J. Geophys. Res.*, *93*(A10), 11455–11472, doi:10.1029/JA093iA10p11455.
Inan, U. S., J. V. Rodriguez, and V. P. Idone (1993), VLF signatures of lightning-induced heating and ionization of the nighttime *D*-region, *Geophys. Res. Lett.*, *20*(21), 2355–2358, doi:10.1029/93GL02620.
Inan, U. S., T. F. Bell, V. P. Pasko, D. D. Sentment, E. M. Wescott, and W. A. Lyons (1995), VLF signatures of ionospheric disturbances associated with sprites, *Geophys. Res. Lett.*, *22*(24), 3461–3464, doi:10.1029/95GL03507.
Inan, U. S., V. P. Pasko, and T. F. Bell (1996), Sustained heating of the ionosphere above thunderstorms as evidenced in "early/fast" VLF events, *Geophys. Res. Lett.*, *23*(10), 1067–1070, doi:10.1029/96GL01360.
Johnsen, R. (1993), Electron-temperature dependence of the recombination of $H_3O^+ \cdot (H_2O)_n$ ions with electrons, *J. Chem. Phys.*, *98*(7), 5390–5395.
Kossyi, I., A. Kostinsky, A. Matveyev, and V. Siulakov (1992), Kinetic scheme of the non-equilibrium discharge in nitrogen-oxygen mixtures, *Plasma Sources Sci. Technol.*, *1*, 207–220.
Kotovsky, D. A., and R. C. Moore (2015), Classifying onset durations of early VLF events: Scattered field analysis and new insights, *J. Geophys. Res. Space Physics*, *120*, 6661–6668, doi:10.1002/2015JA021370.
Kotovsky, D. A., and R. C. Moore (2016), Photochemical response of the nighttime mesosphere to electric field heating—Recovery of electron density enhancements, *Geophys. Res. Lett.*, *43*(3), 952–690.
Leu, M. T., M. A. Biondi, and R. Johnsen (1973), Measurements of the recombination of electrons with $H_3O^+ \cdot (H_2O)_n$-series ions, *Phys. Rev. A.*, *7*(1), 292–298.
Li, J., S. Cummer, G. Lu, and L. Zigoneanu (2012), Charge moment change and lightning-driven electric fields associated with negative sprites and halos, *J. Geophys. Res.*, *117*, A09310, doi:10.1029/2012JA017731.
Liu, N. (2012), Multiple ion species of fluid modeling of sprite halos and the role of electron detachment of O^- in their dynamics, *J. Geophys. Res.*, *117*, A03308, doi:10.1029/2011JA017062.
Lu, G., et al. (2013), Coordinated observations of sprites and in-cloud lightning flash structure, *J. Geophys. Res. Atmos.*, *118*, 6607–6632, doi:10.1002/jgrd.50459.
Lyons, W. A. (1996), Sprite observations above the U.S. High Plains in relation to their parent thunderstorm systems, *J. Geophys. Res.*, *101*(D23), 29,641–29,652.
Meier, R. R. (1969), Balmer alpha and Lyman beta in the hydrogen geocorona, *J. Geophys. Res.*, *74*(14), 3651–3574.
Meieir, R. R., and P. Mange (1970), Geocoronal hydrogen: An analysis of the Lyman-alpha airglow observed from OGO-4, *Planet. Space Sci.*, *13*, 803–821.
Meier, R. R., and P. Mange (1973), Spatial and temporal variations of the Lyman-alpha airglow and related atomic hydrogen distributions, *Planet. Space. Sci.*, *21*, 309–327.
Mitra, A. P. (1975), *D*-region in disturbed conditions, including flares and energetic particles, *J. Atmos. Terr. Phys.*, *37*, 895–913.
Miyasato, R., M. J. Taylor, H. Fukunishi, and H. C. Stenbaek-Nielsen (2002), Statistical characteristics of sprite halo events using coincident photometric and imaging data, *Geophys. Res. Lett.*, *29*, 2033.

Miyasato, R., H. Fukunishi, Y. Takahashi, and M. J. Taylor (2003), Energy estimation of electrons producing sprite halos using array photometer data, *J. Atmos. Sol. Terr. Phys.*, *65*, 573–581.
Moudry, D., H. Stenbaek-Nielsen, D. Sentman, and E. Wescott (2003), Imaging of elves, halos, and sprite initiation at 1ms time resolution, *J. of Atmo. And Sol.-Terr. Phys.*, *65*, 509–518.
Newsome, R. T., and U. S. Inan (2010), Free-running ground-based photometric array imaging of transient luminous events, *J. Geophys. Res.*, *115*, A00E41, doi:10.1029/2009JA014834.
Ogawa, T., and T. Shimazaki (1975), Diurnal variations of odd nitrogen and ionic densities in the mesosphere and lower thermosphere: Simultaneous solution of the photochemical-diffusive equations, *J. Geophys. Res.*, *80*(28), 3945–3960.
Pasko, V. P., U. S. Inan, T. F. Bell, and Y. N. Taranenko (1997), Sprites produced by quasi-electrostatic heating and ionization in the lower ionosphere, *J. Geophys. Res.*, *102*(A3), 4529–4561.
Pasko, V. P., M. A. Stanley, J. D. Mathews, U. S. Inan, and T. G. Woods (2002), Electrical discharge from a thundercloud top to the lower ionosphere, *Nature*, *416*, 152–154, doi:10.1038/416152a.
Peterson, J. R., et al. (1998), Dissociative recombination and excitation of N_2^+: Cross sections and product branching ratios, *J. Chem. Phys.*, *108*(5), 1978.
Picone, J. M., A. E. Hedin, D. P. Drob, and A. C. Aikin (2002), NRLMSISE-00 empirical model of the atmosphere: Statistical comparisons and scientific issues, *J. Geophys. Res.*, *107*(A12), 1468.
Porter, H. S., C. H. Jackman, and A. E. S. Green (1976), Efficiencies for the production of atomic nitrogen and oxygen by relativistic proton impact in air, *J. Chem. Phys.*, *65*(1), 154–167.
Rapp, D., and D. D. Briglia (1965), Total cross sections for ionization and attachment in gases by electron impact, II. Negative-ion formation, *J. Chem. Phys.*, *43*(5), 1480–1489.
Rapp, D., and P. E. Golden (1965), Total cross sections for ionization and attachment in gases by electron impact. I. Positive ionization, *J. Chem. Phys.*, *44*(5), 1464–1479.
Rapp, D., P. E. Golden, and D. D. Briglia (1965), Cross sections for dissociative ionization of molecules by electron impact, *J. Chem. Phys.*, *42*(12), 4081–4085.
Rayment, S. W., and J. L. Moruzzi (1978), Electron detachment studies between O ions and nitrogen, *Int. J. Mass. Spec. Ion Phys.*, *26*, 321–326.
Reid, G. C. (1977), The production of water-cluster positive ions in the quiet daytime *D* region, *Planet. Space Sci.*, *25*, 275–290.
Rowe, J. N., A. P. Mitra, A. J. Ferraro, and H. S. Lee (1974), An experimental and theoretical study of the *D*-region—II. A semi-empirical model for mid-latitude *D*-region, *J. Atmos. Terr. Phys.*, *36*, 755–785.
São Sabbas, F. T., D. D. Sentman, E. M. Wescott, O. Pinto Jr., O. Mendes Jr., and M. J. Taylor (2003), Statistical analysis of space-time relationship between sprites and lightning, *J. of Atmo. And Sol. Terr. Phys.*, *65*, 525–535.
Sentman, D. D., H. C. Stenbaek-Nielsen, M. G. McHarg, and J. S. Morrill (2008), Plasma chemistry of sprite streamers, *J. Geophys. Res.*, *113*, D11112, doi:10.1029/2007JD008941.
Sheehan, C. H., and J.-P. St.-Maurice (2004), Dissociative recombination of N_2^+, O_2^+, and NO^+: Rate coefficients for ground state and vibrationally excited ions, *J. Geophys. Res.*, *109*, A03302, doi:10.1029/2003JA010132.
Smith, D., and M. J. Church (1976), Binary ion-ion recombination coefficients determined in a flowing afterglow plasma, *Int. J. Mass. Spec. Ion Phys.*, *19*, 185–200.
Smith, D., and M. J. Church (1977), Ion-ion recombination rates in Earth's atmosphere, *Planet. Space Sci.*, *25*, 433–439.
Smith, D., N. G. Adams, and M. J. Church (1976), Mutual neutralization rates of ionospherically important ions, *Planet. Space Sci.*, *24*, 697–703.
Spjeldvik, W. N., and R. M. Thorne (1975), The cause of storm after effects in the middle latitude *D*-region, *J. Atmos. Terr. Phys.*, *31*, 1311–1322.
Stenbaek-Nielsen, H. C., D. R. Moudry, E. M. Wescott, D. D. Sentman, and F. T. Sao Sabbas (2000), Sprites and possible mesospheric effects, *Geophys. Res. Lett.*, *27*(23), 2829–3932.
Stenbaek-Nielsen, H. C., and M. G. McHarg (2008), High time-resolution sprite imaging: Observations and implications, *J. Phys. D: Appl. Phys.*, *41*, 234009.
Strobel, D. F., D. M. Hunten, and M. B. McElroy (1970), Production and diffusion of nitric oxide, *J. Geophys. Res.*, *75*(22), 4307–4321.
Strobel, D. F. (1971), Diurnal variation of nitric oxide in the upper atmosphere, *J. Geophys. Res.*, *76*(10), 2441–2452.
Strobel, D. F., and T. R. Young (1974), The nighttime ionosphere: *E* region and lower *F* region, *J. Geophys. Res.*, *79*(22), 3171–3177.
Thomas, G. E. (1963), Lyman alpha scattering in the Earth's hydrogen geocorona, *J. Geophys. Res.*, *68*(9), 2639–2660.
Thomas, L., and M. R. Bowman (1985), Model studies of the *D*-region negative-ion composition during day-time and night-time, *J. Atmos. Terr. Phys.*, *47*(6), 546–556.
van der Velde, O. A., A. Mika, S. Soula, C. Haldoupis, T. Neubert, and U. S. Inan (2006), Observations of the relationship between sprite morphology and in-cloud lightning processes, *J. Geophys. Res.*, *111*, D15203, doi:10.1029/2005JD006879.
van der Velde, O. A., J. Br, J. Li, S. A. Cummer, E. Arnone, F. Zanotti, M. Fllekrug, C. Haldoupis, S. NaitAmor, and T. Farges (2010), Multi-instrumental observations of a positive gigantic jet produced by a winter thunderstorm in Europe, *J. Geophys. Res.*, *115*, D24301, doi:10.1029/2010JD014442.
Velinov, P. (1968), On ionization in the ionospheric *D*-region by galactic and solar cosmic rays, *J. Atmos. Terr. Phys.*, *30*, 1891–1905.
Watanabe, K. (1958), Ultraviolet absorption processes in the upper atmosphere, *Adv. Geophys.*, *5*, 153–221.
Whitten, R. C., and I. G. Poppoff (1965), *Physics of the Lower Ionosphere*, Prentice-Hall, Inc., Englewood Cliffs, N. J.
Williams, E., et al. (2012), Resolution of the sprite polarity paradox: The role of halos, *Radio Sci.*, *47*.
Young, J. M., C. S. Weller, C. Y. Johnson, and J. C. Holmes (1971), Rocket observations of the far UV nightglow at Lyman alpha and shorter wavelengths, *J. Geophys. Res.*, *76*(16), 3710–3722.